

Progress on BaF₂ Crystals and Photosensors

Chih-hsiang Cheng, Bertrand Echenard, Kevin Flood,
Hallmann Gestsson, David Hitlin, Jae Hong Kim, Frank Porter,
Jason Trevor and Ren-Yuan Zhu

July 17, 2015

Abstract

We summarize herein progress on the measurement of barium fluoride crystal properties, including light yield, transmission, radiation hardness and cost, as well as on the development of an avalanche photodiode sensor that is sensitive only to the fast scintillation component of BaF₂.

1 Introduction

The Mu2e calorimeter's purpose is to confirm that the reconstructed track of a muon-to-electron candidate is well measured and defined, and not created by any spurious hit combination within the particle tracker. In order for the calorimeter to better perform this function, faster scintillation crystals are needed. BaF₂ has been identified as the leading choice among the fast scintillators available. Its emission decay has two components: a 0.9 ns fast component and a slower 630 ns component. The fast BaF₂ emission has a peak wavelength of 220 nm, while the slow emission peaks at 300 nm. To take advantage of the fast component at 220 nm, it is necessary to suppress the slow component at 300 nm. This can be done by using solar blind photodetectors, by doping the BaF₂ scintillator to suppress the 300 nm light, or using optical passband filters on the photodetector that strongly attenuate near 300 nm. An appropriate photodetector will need to be large area (of the order of 1 cm²) in order to accommodate the size of the scintillator.

Solar blind large area PMTs are available, however, they are fragile, expensive and cannot be used in magnetic fields. Solid-state wide bandgap solar blind detectors, such as AlGaIn and SiC APDs, are available as well, however, large area detectors have yet to be developed. RMD silicon avalanche photodiodes (APDs) have been identified as a strong photodetector candidate, since they can be fabricated with a large sensing area, ~ 1 cm², are robust and compact, have little dead space, are insensitive to magnetic fields and can be made solar blind by the use of passband filters. However, RMD APDs, like many other silicon based photodetectors, have a relatively low external quantum efficiency (QE) at UV wavelengths.

An APD is essentially a solid state replacement for a PMT and, similar to a PMT, it exhibits gain created by an impact ionization process in the device. APDs are much thinner and more compact than PMTs, and can be easily tiled with little dead space, which increases the system design flexibility. Also, APDs are insensitive to magnetic fields which could be attractive to accelerator experiments where surrounding magnetic fields prevent the use of PMTs. The gain ($\sim 10^3$) of deep-diffused APDs fabricated by RMD is a factor of 10 or more higher compared to that for APDs with reach-through design fabricated by Hamamatsu and PerkinElmer. Device capacitance per unit area and excess noise factor are also lower for RMD's deep-diffused APDs compared to reach-through APDs. The typical UV QE (155-300 nm) is ~ 10 -30%. However, for this application, the UV response and speed of RMD's APD technology needs to be enhanced. Our efforts focus on modifying fabrication of RMDs APDs with JPL's superlattice-doping process and anti-reflection coating technology to improve the APD UV QE and timing properties.

2 Simulation

A series of simulations have been performed to determine the performance of a BaF₂-based or a CsI-based calorimeter. The calorimeter geometry is described in the TDR¹. It is composed of two annular disks separated by 700 mm. The disks have inner and outer radii of 351 mm and 660 mm, respectively. Both BaF₂ and CsI crystals are of hexagonal shape, 33 mm across flats, and 200 mm long. There are a total of 1860 crystals. Two readouts are mounted on each crystal to read the scintillation light. Their characteristics are detailed below.

Event reconstruction in the calorimeter proceeds in several stages. The interaction of the incident particle with the crystals is first simulated by GEANT4, recording the energy, position and time of each step. Each energy deposit is converted into scintillation light, taking into account fluctuations of the photo-statistics and non-uniformity in the longitudinal response. Corrections from non-linearities in the light production have not been implemented yet. The response of each APD is then simulated, including the related electronic noise. A final version of signal digitization and pile-up identification remains to be implemented. To simulate these effects, hits within a given time window, depending on the readout characteristics, are grouped together to form crystal hits. The crystal hit time is set to the time of the first hit, unless a subsequent hit with at least twice the energy of the second most energetic hit is found, in which case the time of that hit is selected.

The crystal hits are then used to form calorimeter clusters. The clustering algorithm starts by taking the crystal hit with the largest energy as seed, and adds all simply connected hits within a time window of ± 10 ns and a threshold in energy of either 3 times the electronic noise or 1 MeV, whichever is larger. The 1 MeV threshold is imposed by the DAQ system limitations. Hits are defined as simply connected if they can be reached through a series of adjacent hits. The procedure is repeated until all crystals hits are assigned to clusters. Additional low-energy deposits that are disconnected from the main cluster are recovered by dedicated algorithms. These fragments are usually produced by the shower, or by low-energy photons emitted by incident particles.

The energy resolution is estimated by simulating conversion electrons distributed at random in the stopping target foils, together with the expected neutron, photon and DIO backgrounds. A few simulations have also been carried out without background to assess its impact on the resolution. For CsI crystals, the photon, neutron and DIO backgrounds simulated by Geant4 (i.e. energy deposits in the crystals) from BaF₂ crystals was used. The conversion of energy deposits into scintillation light and the subsequent steps are performed using CsI crystals. This approximation should have a limited impact on the results. The signal is entirely simulated with CsI crystals.

The fast scintillation light of BaF₂ crystals is read by 9x9 mm² APD with super-layer treatment and atomic layer deposition filter (SL/ALD APD). A UV-extended MPPC with atomic layer deposition filter (ALD MPPC) is also investigated as a possible alternative. The SL/ALD APD has a quantum efficiency (QE) of 50% at 220 nm, following a direct measurement at unity gain, combined with a model that RMD uses to track how the QE improves as the device becomes fully depleted under 1800V bias [1]. The QE of UV-extended MPPC at 220 nm is approximately 20% . The readout selected for CsI crystals is a UV-extended SPL MPPC, with a QE at the level of 40% at 310 nm [3]. The electronic noise has been estimated to be 300 keV/APD for BaF₂ crystals, extrapolated on measurements from LYSO, and 100 keV/MPPC for CsI crystals [2].

The number of photo-electrons per MeV ($N_{p.e./MeV}$) for BaF₂ is derived following a measurement of 160 p.e./MeV for the fast component (220 nm) using a photo-multiplier having a 30% quantum efficiency and a surface of 930 mm² with grease and 8 layers teflon wrapping [4]. A number of 30 photo-electrons per MeV for CsI crystal has been measured using the UV-extended SPL MPPC [3]. The longitudinal response uniformity (LRU) is modeled by a single linear component describing the level of non-uniformity at the end of the crystal w.r.t. its center. A nominal value of 5% is used.

Several simulations are performed for the combinations of crystals and sensors described above. In addition, we study the sensitivity of the results to the integration time, light yield, electronic noise and

¹Although the geometry has evolved since the TDR, the complete set of backgrounds has not been regenerated for the newer designs. Since the background plays an important contribution to the resolution, we needed to use the TDR geometry for these studies.

longitudinal response uniformity for BaF₂ crystals with SL/ALD APD and CsI crystals with MPPC. The complete set of parameters are summarized in Table 1 and 2. We also perform a few simulations without background to assess its effect on the resolution.

Sim. number	Readout type	Integration time (ns)	$N_{p.e./MeV}$ per readout	Noise (keV)	LRU (%)	Other
1	SL/ALD APD	60	23	300	5	default
2	SL/ALD APD	60	15	450	5	
3	SL/ALD APD	60	10	700	5	
4	SL/ALD APD	60	8	900	5	
5	SL/ALD APD	60	23	200	5	
6	SL/ALD APD	60	23	400	5	
7	SL/ALD APD	60	23	1000	5	
8	SL/ALD APD	60	23	2000	5	
9	SL/ALD APD	60	23	300	15	
10	SL/ALD APD	60	23	300	25	
11	SL/ALD APD	60	23	300	5	Bkg x2
12	SL/ALD APD	60	23	300	5	Bkg x4
13	SL/ALD APD	60	23	300	5	$E_{cut,cluster} = 1.5$
14	SL/ALD APD	60	23	300	5	$E_{cut,cluster} = 2.0$
100	ALD VUV MPPC	150	16	200	5	
200	SL/ALD APD	60	23	300	5	No Bkg
201	SL/ALD APD	60	23	300	5	No Bkg, $E_{cut,cluster} = 1.5$
202	SL/ALD APD	60	23	300	5	No Bkg, $E_{cut,cluster} = 2.0$

Table 1: Parameters of the simulations performed for BaF₂ crystals with background. The number of p.e./MeV and the noise are given per readout. Two readouts are mounted on each crystal. The variable $E_{cut,cluster}$ denotes minimum energy required for a hit to be included in the cluster (see related discussion on cluster reconstruction above).

The distribution of the difference between the reconstructed cluster energy and the true signal electron energy, $\Delta E = E_{clu} - E_{trk}$, are shown in Figure 1 for a few simulations. This variable accounts for the energy lost by the electron before hitting the calorimeter. The high-side tail is due to background pile-up with the cluster. An unbinned likelihood fit to the data with a Crystal Ball function (Gaussian function with a power-law tail) is performed to extract the resolution. The core resolution (Gaussian component) and the FWHM/2.35 are reported in Table 3 and 4. The quoted uncertainties are only statistical, and systematic uncertainties due to the choice of the fit model could be as large as the statistical components for some configurations.

The core resolution and FWHM/2.35 for the BaF₂ crystals with SL/ALD APD (CsI crystal with MPPC) are 3.6 ± 0.2 MeV (4.2 ± 0.3 MeV) and 4.4 ± 0.3 MeV (5.7 ± 0.3 MeV), respectively. The comparison of the two ΔE spectra are shown in Figure 2. The resolution for CsI is about 10% larger, mostly due to the effect of additional noise integrated over a longer time window compared to barium fluoride. Improved treatment of the waveform digitization and hit extraction should partially alleviate this difference. We also note that the different readouts for BaF₂ crystals yield fairly similar results; the SL/ALD APD performing a bit better than the UV-extended ALD MPPC.

The dependence on the light yield, longitudinal response uniformity and readout noise are displayed in Figure 3 and 4. As expected, the resolution degrades with the decrease of the light yield, the longitudinal response uniformity, or the electronic noise. The resolutions remains in an acceptable range, except in the of large APD noise (larger than 1 MeV). In this case, the CsI based calorimeter seems to be a better alternative.

The impact of the level of background is shown in Figure 5. Increasing the background by a factor of

Sim. number	Readout type	Integration time (ns)	$N_{p.e./MeV}$ per readout	Noise (keV)	LRU	Other
1	MPPC	150	30	100	5	default
2	MPPC	150	20	150	5	
3	MPPC	150	15	200	5	
4	MPPC	150	10	300	5	
5	MPPC	150	30	100	15	
6	MPPC	150	30	100	25	
7	MPPC	60	30	100	5	T_{int} of BaF ₂
8	MPPC	150	30	100	5	Bkg x2
9	MPPC	150	30	100	5	Bkg x4
10	MPPC	150	30	100	5	$E_{\text{cut},\text{cluster}} = 1.5$ MeV
11	MPPC	150	30	100	5	$E_{\text{cut},\text{cluster}} = 2.0$ MeV
200	MPPC	150	30	100	5	No bkg
201	MPPC	150	30	100	5	No bkg, $E_{\text{cut},\text{cluster}} = 1.5$
202	MPPC	150	30	100	5	No bkg, $E_{\text{cut},\text{cluster}} = 2.0$

Table 2: Parameters of the simulations performed for CsI crystals with background. The number of p.e./MeV and the noise are given for a single readout. Two readouts are used per crystal. The variable $E_{\text{cut},\text{cluster}}$ denotes minimum energy required for a hit to be included in the cluster (see discussion above).

four ² results in a $\sim 30\%$ ($\sim 40\%$) increase of the resolution for barium fluoride (cesium iodine) crystals. A naive linear extrapolation gives a resolution (FWHM/2.35) around 8 MeV for BaF₂ and 14 MeV for CsI for a tenfold background increase. The effect of varying the threshold in energy in the clustering algorithm from 1.0 MeV to 2.0 MeV is illustrated in Figure 6, for simulations with and without background. Once again, the impact on the resolution is small.

Finally, we show the signal acceptance in Figure 7, defined as the number of events having a reconstructed track and an electromagnetic cluster above a given energy threshold normalized to the number of events containing a reconstructed track. Since the absolute value of energy spectra are not properly calibrated yet, the peak of each cluster energy distribution is arbitrarily set to 100 MeV. An efficiency slightly above to 90% (65%) is observed for cluster energies above 60 MeV (90 MeV). The differences in efficiency between BaF₂ and CsI are partly due to the crude hit extraction procedure.

²Not enough background was generated to simulate a factor 10 increase.

Sim. number	Readout	T_{int} (ns)	$N_{p.e./MeV}$	Noise (keV)	σ (MeV)	FWHM/2.35 (MeV)	other
1	SL/ALD APD	60	23	300	3.6 ± 0.2	4.4 ± 0.2	default 15% LRU 25% LRU Bkg x2 Bkg x4 $E_{\text{cut},\text{cluster}} = 1.5$ $E_{\text{cut},\text{cluster}} = 2.0$
2	SL/ALD APD	60	15	450	4.1 ± 0.2	4.4 ± 0.2	
3	SL/ALD APD	60	10	700	4.4 ± 0.4	5.1 ± 0.3	
4	SL/ALD APD	60	8	900	5.3 ± 0.3	5.7 ± 0.2	
5	SL/ALD APD	60	23	200	3.3 ± 0.2	4.0 ± 0.2	
6	SL/ALD APD	60	23	400	4.0 ± 0.2	4.6 ± 0.2	
7	SL/ALD APD	60	23	1000	5.9 ± 0.4	6.9 ± 0.3	
8	SL/ALD APD	60	23	2000	7.6 ± 1.0	8.8 ± 0.5	
9	SL/ALD APD	60	23	300	3.9 ± 0.2	4.7 ± 0.2	
10	SL/ALD APD	60	23	300	4.3 ± 0.4	5.6 ± 0.2	
11	SL/ALD APD	60	23	300	4.2 ± 0.2	4.9 ± 0.2	
12	SL/ALD APD	60	23	300	5.5 ± 0.3	5.8 ± 0.3	
13	SL/ALD APD	60	23	300	4.0 ± 0.2	4.7 ± 0.2	
14	SL/ALD APD	60	23	300	4.0 ± 0.2	4.6 ± 0.2	
100	ALD VUV MPPC	150	16	200	4.2 ± 0.4	5.2 ± 0.3	
200	SL/ALD APD	60	23	300	2.2 ± 0.1	2.9 ± 0.1	No Bkg
201	SL/ALD APD	60	23	300	2.8 ± 0.1	3.2 ± 0.1	No Bkg, $E_{\text{cut},\text{cluster}} = 1.5$
202	SL/ALD APD	60	23	300	2.7 ± 0.1	3.4 ± 0.1	No Bkg, $E_{\text{cut},\text{cluster}} = 2.0$

Table 3: The core resolution (σ) and the FWHM/2.35 extracted from the fits to the different simulations for BaF₂ crystals. The number of p.e./MeV and the noise are given per readout.

Sim. number	Readout type	T_{int} (ns)	$N_{p.e./MeV}$	Noise (keV)	core resolution σ (MeV)	FWHM/2.35 (MeV)	other
1	MPPC	150	30	100	4.2 ± 0.3	5.7 ± 0.3	default 15% LRU 25% LRU T_{int} of BaF ₂ Bkg x2 Bkg x4 $E_{\text{cut},\text{cluster}} = 1.5$ $E_{\text{cut},\text{cluster}} = 2.0$
2	MPPC	150	20	150	4.1 ± 0.4	6.0 ± 0.3	
3	MPPC	150	15	200	4.3 ± 0.4	5.9 ± 0.2	
4	MPPC	150	10	300	5.6 ± 0.4	6.4 ± 0.4	
5	MPPC	150	30	100	5.1 ± 0.4	6.6 ± 0.3	
6	MPPC	150	30	100	5.2 ± 0.5	6.4 ± 0.4	
7	MPPC	60	30	100	3.7 ± 0.3	4.5 ± 0.2	
8	MPPC	150	30	100	5.1 ± 0.5	6.6 ± 0.3	
9	MPPC	150	30	100	7.6 ± 0.7	8.9 ± 0.6	
10	MPPC	150	30	100	4.6 ± 0.4	6.3 ± 0.3	
11	MPPC	150	30	100	4.4 ± 0.4	6.0 ± 0.3	
200	MPPC	60	30	100	2.5 ± 0.1	3.5 ± 0.1	No Bkg
201	MPPC	60	30	100	2.9 ± 0.1	3.7 ± 0.1	No Bkg, $E_{\text{cut},\text{cluster}} = 1.5$
202	MPPC	60	30	100	3.4 ± 0.1	4.0 ± 0.1	No Bkg, $E_{\text{cut},\text{cluster}} = 2.0$

Table 4: The core resolution (σ) and the FWHM/2.35 extracted from the fits to the different simulations for CsI crystals. The number of p.e./MeV and the noise are given per readout.

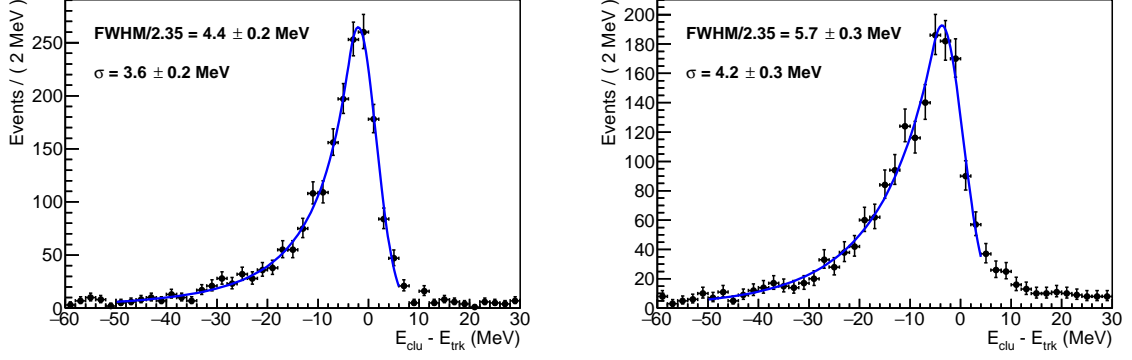


Figure 1: Left: Fit to the difference between the true signal electron energy and the reconstructed cluster energy, $E_{clu} - E_{trk}$, for BaF₂ crystal with SL/ALD APD (simulation 1). Right: Same distribution for Csi crystal with MPPC (simulation 1).

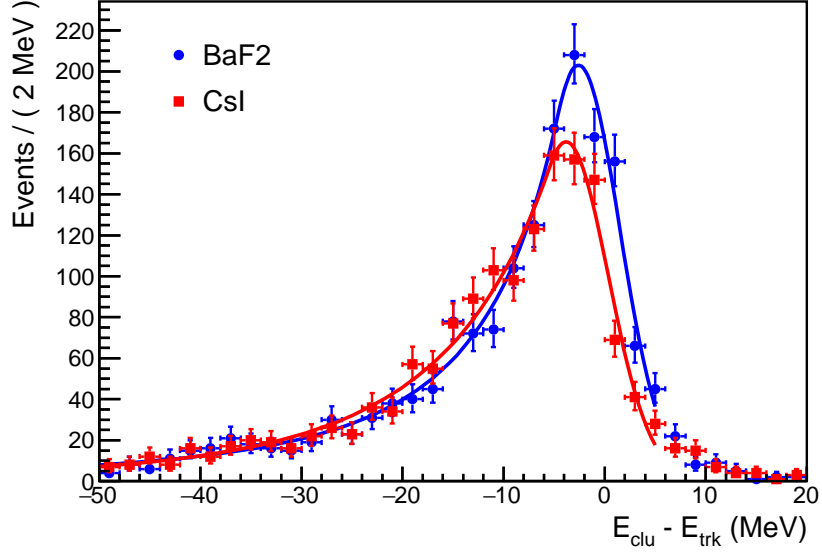


Figure 2: Left: Comparison of the difference between the true signal electron energy and the reconstructed cluster energy, $E_{clu} - E_{trk}$, for BaF₂ with SL/ALD APD (simulation 1) and Csi with MPPC (simulation 1).

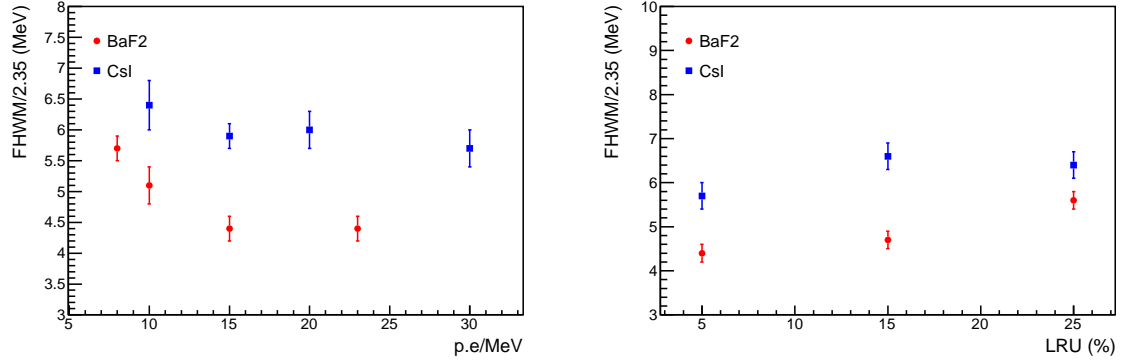


Figure 3: Left: Distribution of the FWHM/2.35 as a function of the number of p.e./MeV for BaF₂ (red) and CsI (blue) crystals. Right: Distribution of the FWHM/2.35 as a function of longitudinal response uniformity (LRU) for BaF₂ (red) and CsI (blue) crystals.

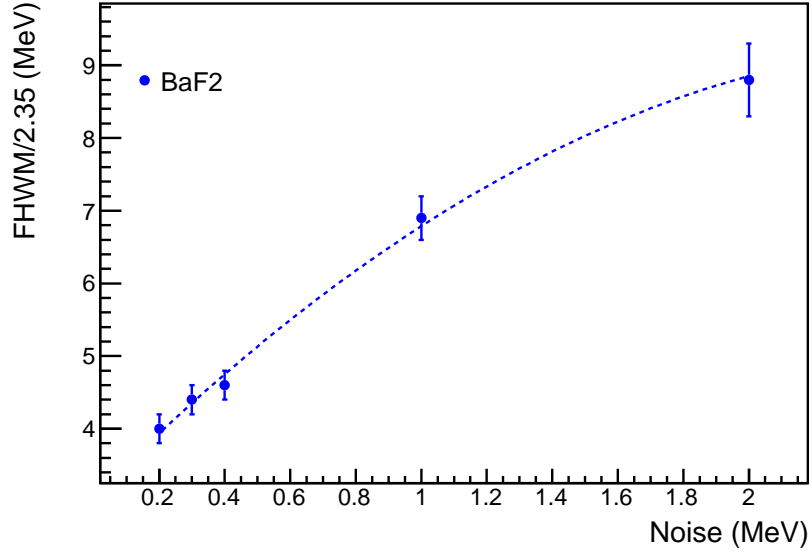


Figure 4: Distribution of the FWHM/2.35 as a function of the readout noise for BaF₂ crystals, together with a fit using a second-order polynomial (dashed line). The resolution FWHM/2.35 for CsI is at the level of ~ 6 MeV.

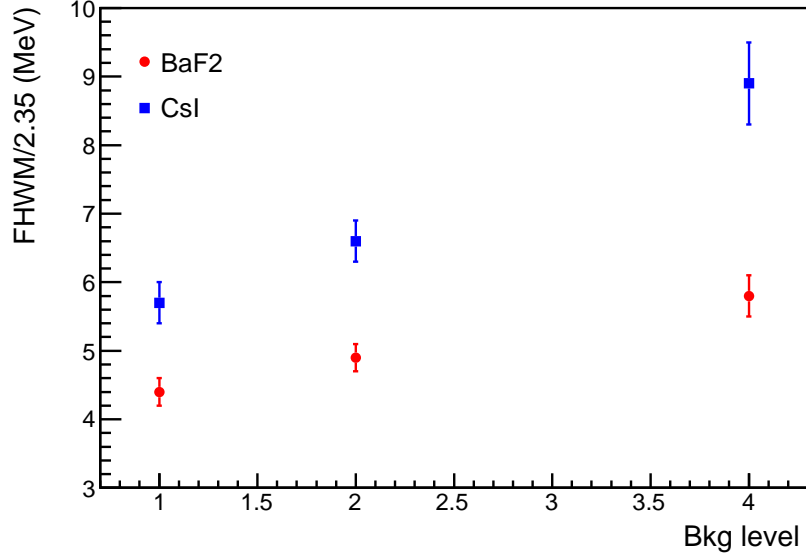


Figure 5: Distribution of the FWHM/2.35 as a function of the background level for BaF₂ (red) and CsI (blue) crystals.

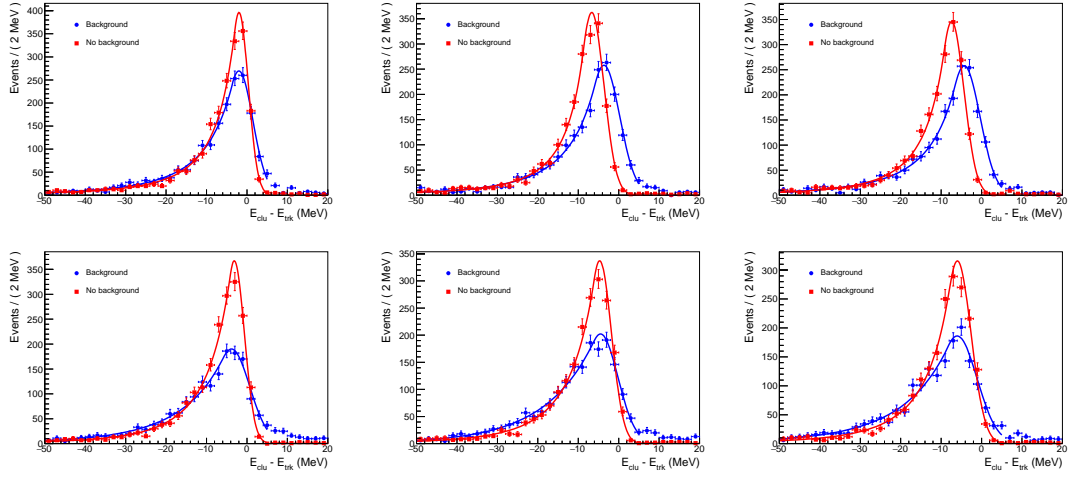


Figure 6: Top: Fits to the difference between the true signal electron energy and the reconstructed cluster energy, $E_{clu} - E_{trk}$, for BaF₂ crystals with / without background for different values of energy cut in the clustering algorithm: 1.0 MeV (left), 1.5 MeV (middle) and 2.0 MeV (right). Bottom: Same distributions for CsI crystals.

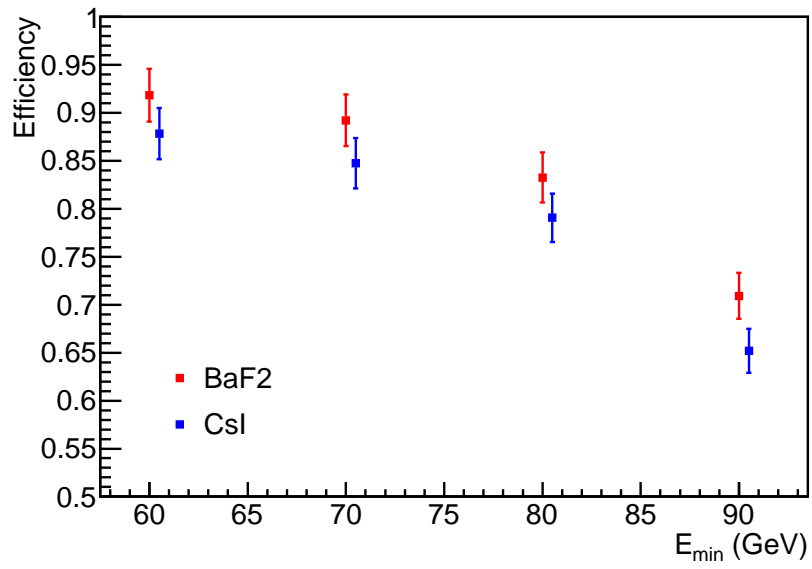


Figure 7: Efficiency as a function of the cut on the cluster energy for BaF₂ (red) and CsI (blue) crystals. The efficiency is defined as the number of events having a reconstructed track and an electromagnetic cluster above a given energy threshold normalized to the number of events containing a reconstructed track. The peak of each cluster energy distribution is arbitrarily set to 100 MeV.

3 Energy calibration

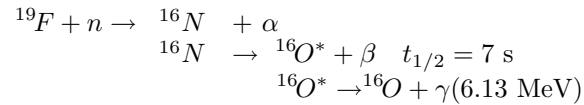
The calorimeter requirements relevant to energy calibration are:

- Provide online calibration sufficient for calorimeter trigger.
- Precision commensurate with calorimeter resolution requirement of $\sigma_E \equiv \text{FWHM}/2.35 \sim 5\%$ at 100 MeV.
- Absolute precision and stability better than 1%.
 - Absolute scale independent of tracker.
- Because the crystals are different, an independent calibration is required for each crystal.
- Light output is time-dependent, hence the time-dependence must be tracked (over a scale of weeks).
- Perform a (source) calibration of entire calorimeter in ~ 10 minutes.

The calibration tools that we have available include:

1. Electronics pulser (FEE)
2. Temperature monitoring
3. Light flasher system
4. Source calibration system, 6.13 MeV
5. Decays in orbit
 - Compare with tracker
 - Different B fields for different momentum ranges
 - Absolute spectrum well known at mid-energies
6. Cosmic rays
7. 70 MeV e^+ from $\pi^+ \rightarrow e^+ \nu_e$

The 6 MeV source calibration system produces 6 MeV photons from excited oxygen-16 produced via neutron activation of fluorine in the chain:



The source is in a bunker off-detector, where the neutrons are produced with a DT generator with approximately 14 MeV kinetic energy. Fluorinert (3M's FC-770) provides the fluorine. It is activated in a bath around the DT generator, and the fluid is pumped to thin-wall aluminum tubing at the faces of the two calorimeter disks.

The basic strategy for calibration is as follows: The initial crystal-by-crystal calibration is performed using the 6 MeV source. We plan to do this pre-installation, and then of order once every week during operation of the experiment. This calibration will serve as the online calibration, in the calorimeter trigger.

Higher energy with electrons from muons decaying in orbit (DIOs) Interpolation and extrapolation with source [Tracker could be used]

Absolute spectrum (at lower fields) Check of MC extrapolation

Monitor electronic gains with pulser Monitor APD temperature Monitor crystal transmission with light pulser

Investigate maintaining detailed crystal-by-crystal time-dependent model in MC using calibration and monitoring data

Cosmic rays as independent check

$\pi^+ \rightarrow e^+ \nu_e$ as independent check

4 Barium fluoride characteristics

The existence of the very fast scintillation component in BaF_2 makes this crystal an attractive candidate for high rate applications such as the Mu2e calorimeter, in both its initial and possible upgrade phases. The BaF_2 scintillation spectrum is shown in Figure 8. BaF_2 was thoroughly investigated as a candidate for the calorimeter of the GEM detector at the SSC[?] more than two decades ago, and has, in fact, been employed in the TAPS experiment[?] at Mainz, which does not have a magnetic field. For Mu2e to make full use of the high rate capability afforded by the fast decay time component at 220 nm, however, requires a means of rejecting the much more intense slow component at 300 nm with a readout device that can operate in a 1T magnetic field. Solar blind photomultipliers have adequate quantum efficiency at 220 nm, and some rejection at 300 nm, but are not suitable for use in a magnetic field.

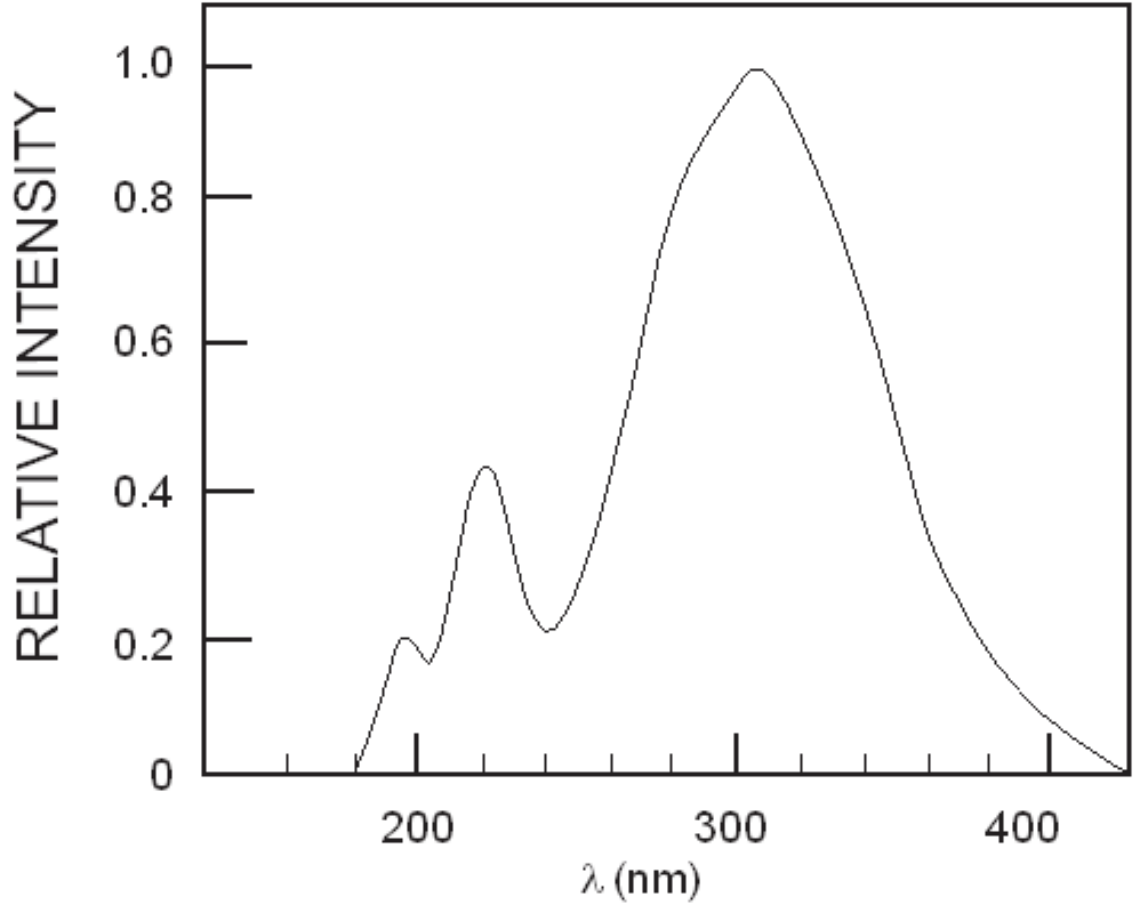


Figure 8: The BaF_2 fast scintillation component at 220 nm comprises $\sim 15\%$ of the light, the slow component at 300nm, $\sim 85\%$

There are approaches to making use of the fast 220 nm component of BaF₂: reducing the size of the 300 nm component through doping and/or finding a suitable readout device that is insensitive to the slow component while retaining adequate quantum efficiency for the fast component. It is possible to reduce the 300 nm emission component without too much effect on the 220 nm component by doping with rare earths such as lanthanum[?], but this is not a large enough reduction to solve the problem at hand. We have begun a study of this type of doping, mainly aimed at understanding the radiation hardness of dope BaF₂ crystals.

Our main focus has been on developing UV sensitive solid state photosensors. There are commercial devices with extended UV response, but no large area devices that can discriminate between the wavelengths of the fast and slow components of BaF₂ emission. We have thus formed a Caltech/JPL/RMD collaboration to develop such a device.

A more detailed

5 Photosensors

5.1 Superlattice deposition

Typical large area APDs have poor quantum efficiency in the BaF₂ spectral region. However, APDs and SiPMs/MPPCs from Hamamatsu and RMD made without the normal protective epoxy coating, and therefore somewhat fragile, have quantum efficiencies in the 200 nm region of 17% [?]. These devices cannot, however, discriminate between the 220 nm fast component and 300 nm slow components of BaF₂. The presence of the slow component limits the rate capability of the calorimeter, and can therefore be an issue in high background conditions.

Our approach is to transform a large-area (9×9 mm²) RMD APD [?], which has high gain (up to 2000) and low capacitance 0.7pf/mm², into a superlattice-doped APD [?] and to incorporate an atomic layer deposition (ALD) antireflection filter [?] that provides 60% quantum efficiency at 220 nm and 0.1% efficiency at 300 nm, thereby enabling us to obtain a larger number of photoelectrons/MeV, and also to take full advantage of the fast decay time component of BaF₂.

Superlattice (2D) doping, a JPL-developed surface passivation technique, produces stable surfaces on silicon photosensors. These techniques were developed to overcome surface damage due to ultraviolet radiation in satellite instrumentation. The subsurface structures are formed using a combination of molecular beam epitaxy and controlled crystalline silicon growth. After growing a thin layer of undoped silicon, a monolayer of boron is deposited, then another silicon layer is grown, and the process is repeated up to four times. The resulting subsurface structure, with high quality self-organized layers of boron atoms at densities of $\sim 2 \times 10^{14}/\text{cm}^2$ (see Figure 9),

The reason for the low QE achieved by most solid state devices in the UV region is two-fold: in typical devices there is an undepleted region of tens of microns between the Si/SiO₂ passivation region on the absorbing surface and the depletion region that is in close proximity to the avalanche region. Due to quantum exclusion, the superlattice structure suppresses recombination of charge at the surface, thereby improving the QE in the 220 nm region to close to the theoretical maximum. The greatly reduced undepleted region of the superlattice-doped device also produces substantially improved timing characteristics (see Figure 10). Second, most devices have a protective resin layer that lowers the net quantum efficiency. This layer is not required in our device, which is passivated and protected by the creation of an atomic layer deposition filter described below.

5.2 Atomic layer deposition filter

It then remains to apply a multilayered atomic layer deposition (ALD) coating to serve as a bandwidth-reducing interference and antireflection filter. These films, in our case alternating layers of aluminum and aluminum oxide, are created by forming a series of single atomic layers through self-limiting chemical reactions with the substrate. This process produces uniform pinhole-free layers of precise thickness. Figure 11 shows the calculated transmission of such a filter as a function of wavelength. For a five-layer ALD coating, the QE

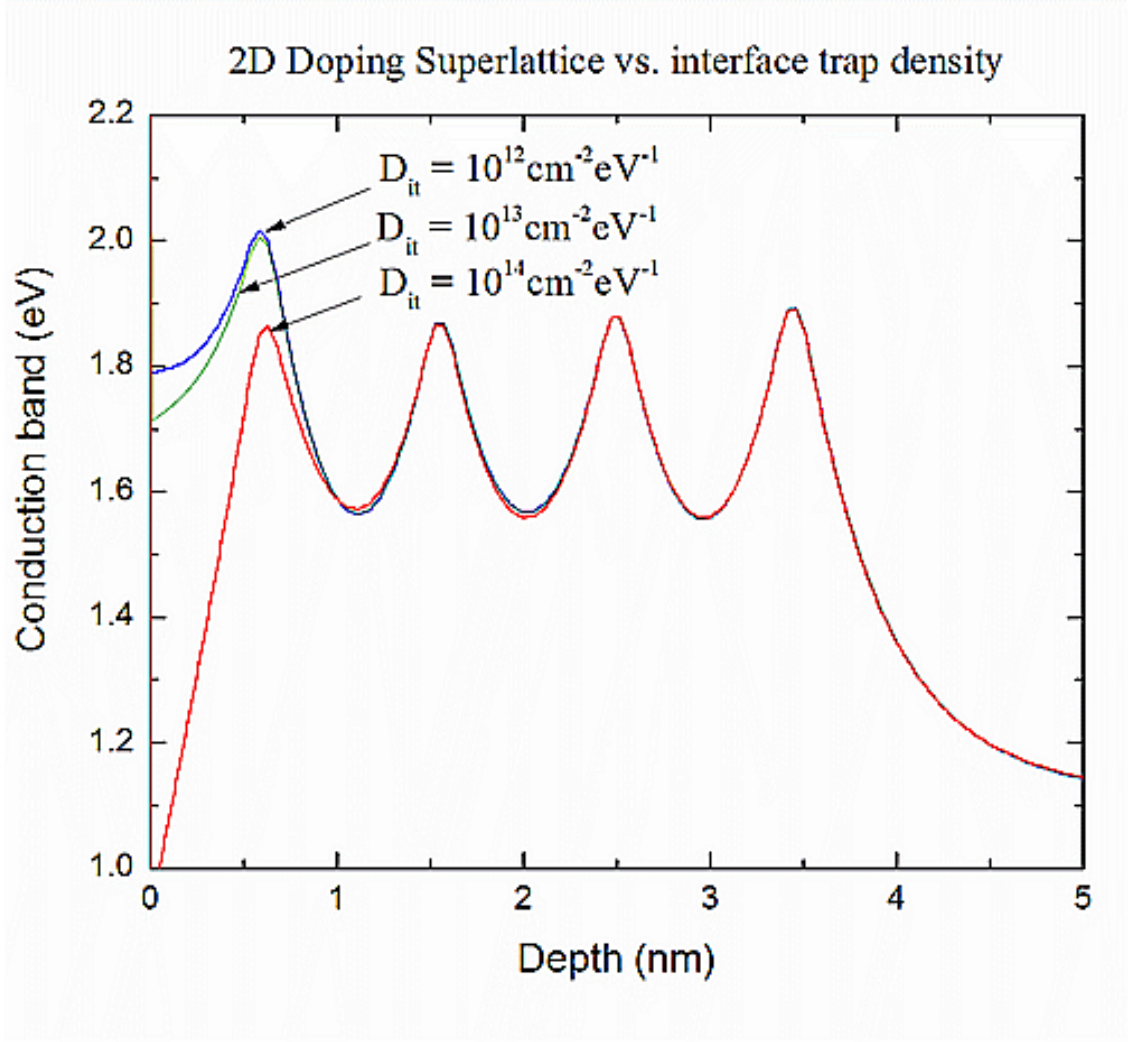


Figure 9: A four-layer superlattice grown by MBE, in which four 2D-doped layers are separated by 1 nm. This 2D doping creates a maximum field of 10^7 V/cm. The 2D doping superlattice forms a surface depletion layer with a fixed width of less than 1 nm, which is stable against interface trap densities in excess of 10^{14} cm^{-3} , enabling the detector to remain stable even when the surface is severely damaged by irradiation by DUV radiation.

at normal incidence for the fast component of BaF_2 is close to 70%, and the extinction at the slow component wavelength is nearly complete. The transmission of the interference filter is a function of incident angle, which is shown in Figure 12.

6 Electrical performance

We have produced several versions of superlattice/ALD-modified RMD APDs thus far. The anticipated filter response and quantum efficiency improvements have been experimentally demonstrated. The devices, however, have somewhat elevated dark current and noise, as seen in Figure 13. Operation at somewhat reduced temperatures improves the noise performance substantially: at $\sim 25^\circ$ below ambient, the noise of the superlattice/ALD-modified devices is equivalent to that of standard devices at room temperature.

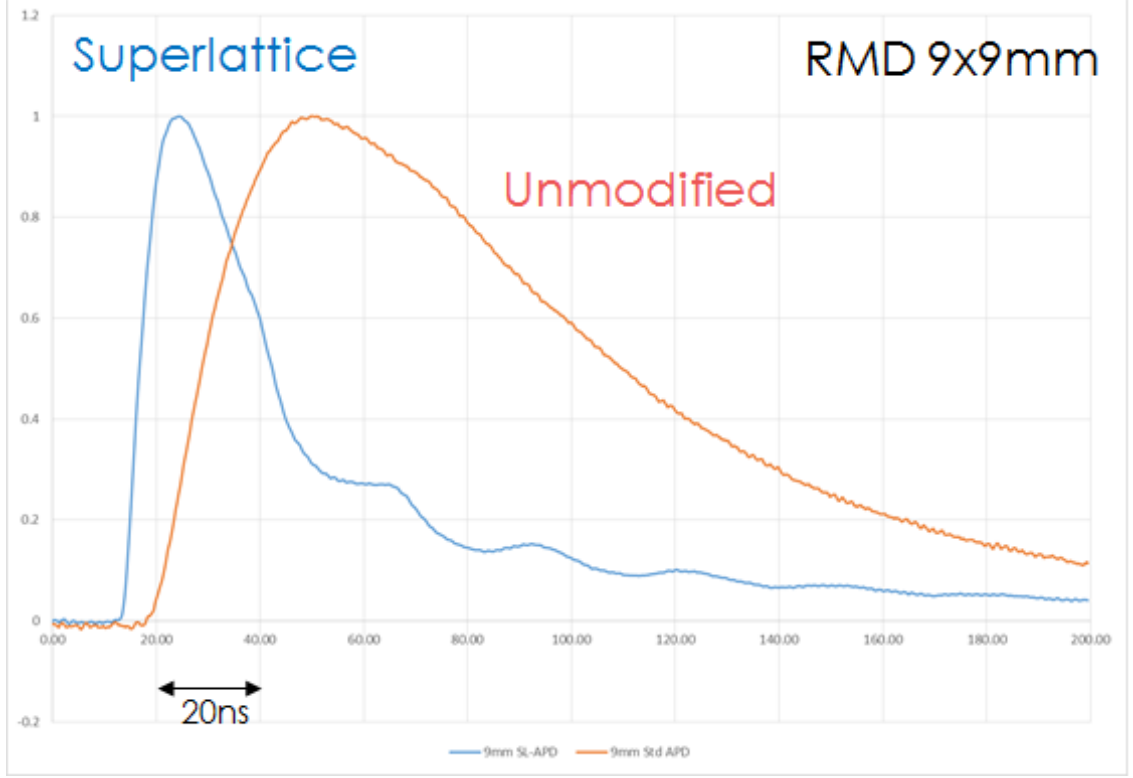


Figure 10: Response of unmodified and superlattice-doped $9 \times 9 \text{ mm}^2$ RMD APDs.

Several process variations are being investigated to reduce the dark current and associated noise. These include variation of the parameters of the superlattice deposition layers, modification of the first dielectric layer of the ALD filter and changes to the electrical contact geometry. The current devices are nonetheless suitable for deployment in the Mu2e calorimeter.

7 Conclusion

References

- [1] M. McClish *et al.*, "Superlattice Doped APDs for Improved UV Sensitivity in Scintillator Calorimetry".
- [2] Mu2e doc-db 5405, p.10
- [3] Mu2e doc-db 5166
- [4] Mu2e doc-db 5716

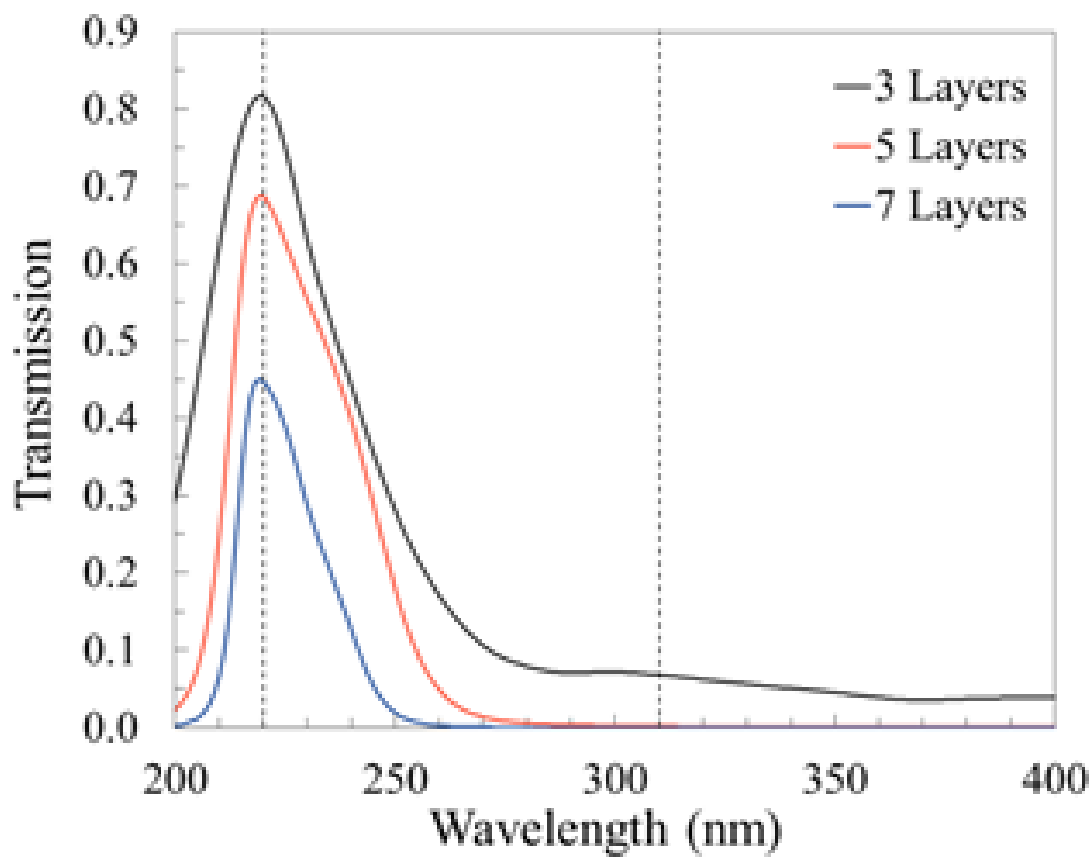


Figure 11: Quantum efficiency (QE) as a function of wavelength for three, five seven layer ALD filters.

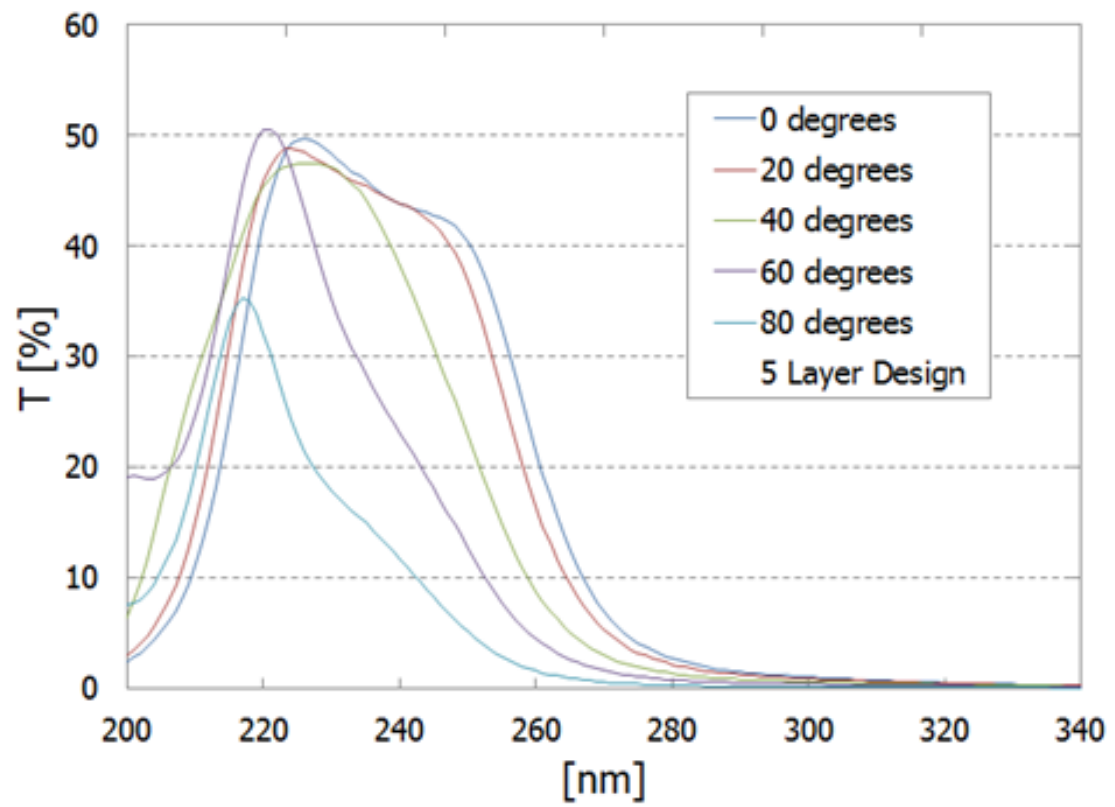


Figure 12: Angular response of the five layer ALD filter as a function of wavelength.

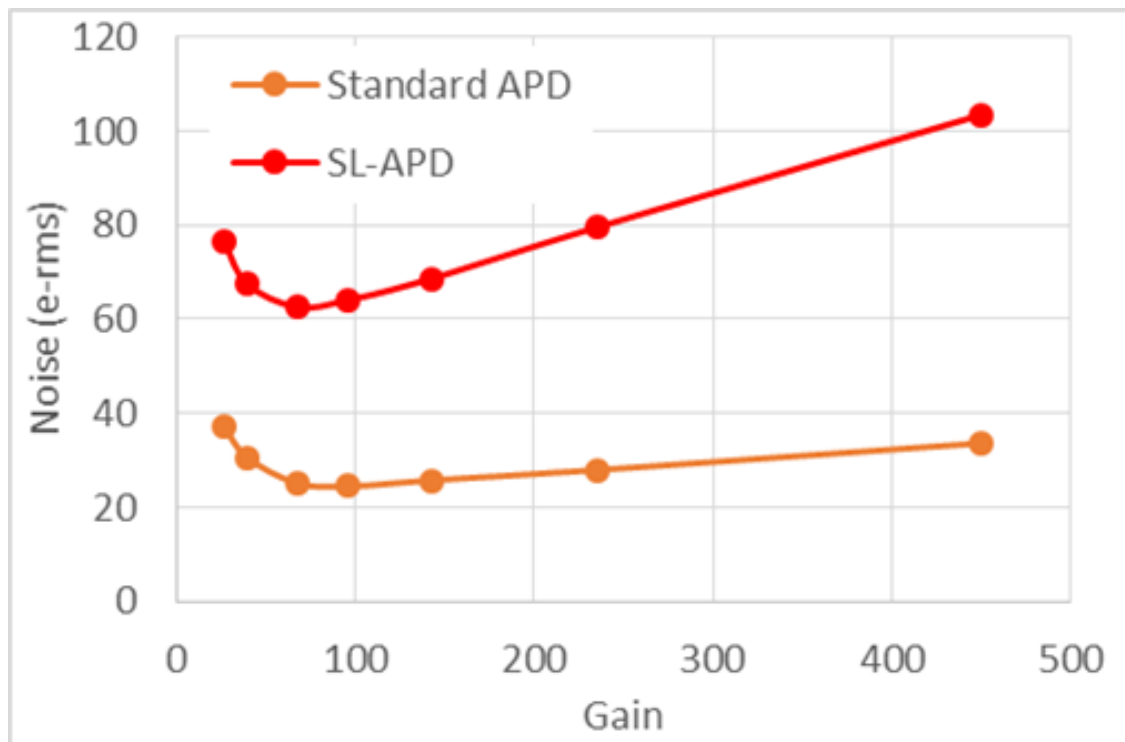


Figure 13: Noise in \hat{r} ms electrons of a standard and a superlattice-doped RMD APD as a function of gain.

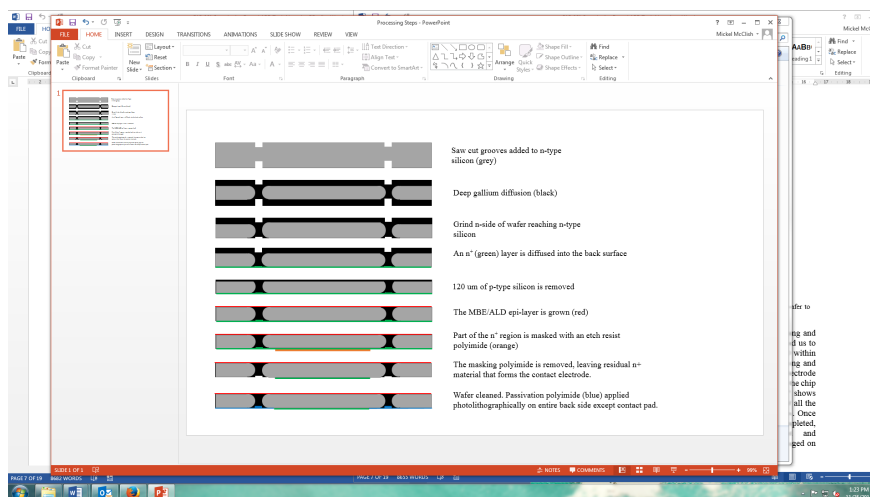


Figure 14: Replace this text with your caption.

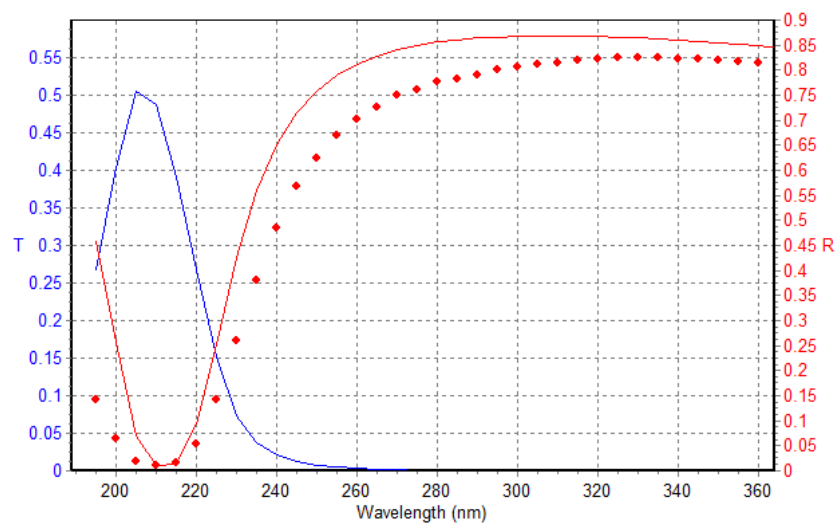


Figure 15: Calculated response of five layer ALD filter.